Delamination of multidirectional composite laminates at 0°/θ° ply interfaces

P. Prombut[a,]*, L. Michel[a], F. Lachaud[a], J.J. Barrau[b]

[a]*Department of Mechanical Engineering, ENSICA, 1 Place Emile Blouin, Toulouse 31056, France*

[b]*Department of Mechanical Engineering, University of Toulouse III, 118 Route de Narbonne, Toulouse 31062, France*

Abstract

The main objective of this study is to develop a methodology for establishing mixed-mode delamination propagation criteria of non-unidirectional laminates. The crack interface was chosen to be 0°/45° and the effort was mainly focused on obtaining the mode I fracture toughness (G_{IC}). The widely used DCB test was avoided due to anticipated problems with intralaminar damage developing at the ply interface of interest. The ADCB and AMMF methods were used to determine the mixed-mode fracture toughness with the largest amount of mode I. The selected stacking sequence resulted in desirable crack propagation behavior; there was no change of delamination plane, an acceptable crack front profile, no initial specimen curvature, and no energy dissipation through global specimen damage. Finite element simulation was found to be the only tool capable of analyzing the experimental data.

Keywords: Delamination; Mixed-Mode; Multidirectional; Damage Mechanics.

1. Introduction

One of the most common damage mechanisms in continuous fiber-reinforced composite laminates is the delamination. It is widely accepted that the approach to characterize the resistance to delamination is by using fracture mechanics. Progress has been made in the development of test methods to measure the interlaminar fracture toughness of composite laminates by determining the critical energy release rate, G_c. The vast majority of the work reported in the literature has focused on unidirectional (UD) materials [1,2]. With fracture toughness tests in mode I, mode II, and mixed-mode I+II, a delamination propagation criterion of a UD laminate can be established [3-6]. However, most structural composite laminates are multidirectional (MD) and delaminations usually develop between plies of different orientations [1,2].

The main objective of this study is to develop a methodology for establishing crack propagation criteria of non-unidirectional laminates. The interface 0°/θ° is preferred because the specimen can be positioned such that only the 0° interfacing ply is under high tension load in mode II and mixed-mode I+II tests [1]. The present work focuses on determining the critical energy release rate in mode I, G_{IC}. Under the conventional Double Cantilever Beam (DCB) test method, non-unidirectional delamination interfaces suffer the change of delamination plane [1,7], which invalidate the test results. The Asymmetric Double Cantilever Beam (ADCB) [4,6,8] and Asymmetric Mixed-Mode Flexure (AMMF) [3,6,9,10] methods are used for the mixed-mode I+II loading with high mode I content in order to determine the G_{IC}.

The delamination interface was chosen to be 0°/45°. The stacking sequence for the specimens was carefully selected using Classical Lamination Theory (CLT) in order to eliminate in-plane coupling and in-plane/out-of-plane coupling. The bending/bending and bending/twisting coupling were also minimized. Studies were performed to minimize the effects of thermal residual stresses on the toughness.

A series of delamination tests was performed on multidirectional specimens made from the unidirectional prepreg of carbon fibers (T700) and a tough epoxy matrix (M21). For a basis of comparison, the DCB, ELS (End Loaded Split), ADCB, MMF, and AMMF tests were performed on UD specimens to create a delamination criterion for 0°/0° interface. The data reduction was based on beam theory and a compliance method. Local and global approaches of mode decomposition are compared for the mixed-mode tests. Finite element simulations were performed to determine the energy release rate (ERR), mode ratio, and global ply damage in the MD specimens.

2. Experimental procedure

2.1. Data reduction

Delamination tests were first performed on 12-ply unidirectional specimens (cured ply thickness 0.26 mm). Specimens with a mid-plane delamination were used for the DCB, ELS, and MMF tests. Those with an asymmetric delamination were for the ADCB and AMMF tests. These specimens were called ADCB12 and AMMF12 to indicate the number of plies that they contain. The thickness ratio of 1/3 was chosen as a compromise between a high mode I content and an adequate bending rigidity of the thinner arm in the AMMF12 specimens. The descriptions and data reduction methods of the tests are as follows:

Mode I: DCB test

A load P is applied to each arm of a specimen with a delamination length a. The deflection of the specimen is measured by the displacement of the crosshead, δ. The energy release rate (ERR) for mode I, G_I, is calculated using the modified beam theory [11-13].

$$G_I = \frac{3P\delta}{2B(a+\chi_I h)} \tag{1}$$

Where B is the specimen width, h the thickness of the specimen arm, and χ_I a correction factor for the beam root rotation.

$$\chi_I = \sqrt{\frac{E_{1f}}{11G_{12}}\left\{3-2\left(\frac{\Gamma}{\Gamma+1}\right)^2\right\}}, \qquad \Gamma = 1.18\frac{\sqrt{E_{1f}E_{22}}}{G_{12}} \tag{2}$$

Where E_{1f}, E_{22}, and G_{12} are the elastic moduli of the material.

The G_I value is then multiplied by the correction factor F which accounts for the shortening of the moment arms and the tilting of the load blocks [13]. The dimension of a load block is shown in Fig. 1.

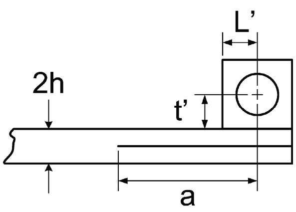

Fig. 1. Load block dimension.

$$F = 1 - \frac{3}{10}\left(\frac{\delta}{a}\right)^2 - \frac{3}{2}\left(\frac{\delta \cdot t}{a^2}\right), \qquad t = t' + \frac{h}{2} \tag{3}$$

Where t' is the distance from the glued surface to the center of the load pin, Fig. 1.

Mode II: ELS test

The specimen is clamped in a support that can slide in the longitudinal direction. The ERR for mode II, G_{II}, is determined from the experimental compliance method [14].

$$G_{II} = \frac{3mP^2a^2}{2B} \tag{4}$$

Where m is the slope of the plot compliance ($C = \delta/P$) versus a^3.

The determination of the specimen shortening is as follows [3]:

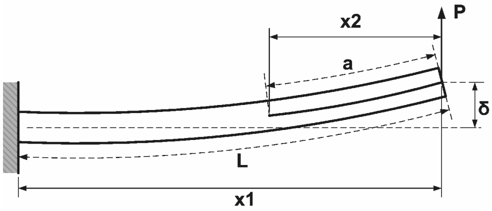

Fig. 2. Specimen shortening in ELS and MMF tests.

$$\frac{x_1}{L} = 1 - \theta_1\left(\frac{\delta}{L}\right)^2 \tag{5}$$

Where $\theta_1 = \frac{3}{10}\cdot\frac{\left\{2+5(\beta-1)X^3+(\beta-1)(2\beta-3)X^5\right\}}{\left\{1+(\beta-1)X^3\right\}^2}$, $\beta = \frac{(h_1+h_2)^3}{h_1^{\,3}+h_2^{\,3}}$, and $X = \frac{a}{L}$

$$\frac{x_2}{a} = 1 - \theta_2\left(\frac{\delta}{L}\right)^2 \tag{6}$$

Where $\theta_2 = \frac{3}{40}\cdot\frac{\left\{15+(20\beta-30)X^2+\left(8\beta^2-20\beta+15\right)X^4\right\}}{\left\{1+(\beta-1)X^3\right\}^2}$

The moment arm shortening is taken into account by replacing the crack length, *a*, in Eq. (4) by the effective moment arm length, x_2 in Eq. (6).

Mixed-mode I+II: MMF test

The MMF method uses the same fixture as the ELS. One arm of the specimen (arm 2) is loaded with the force *P*, while the other arm is free. The G_I and G_{II} are determined from the modified beam theory [3].

$$G_I = \frac{6P^2\left(a+\chi_I h_2\right)^2}{B^2 E_{1f}}\frac{h_1^{\,3}}{h_2^{\,3}\left(h_1^{\,3}+h_2^{\,3}\right)} \tag{7}$$

$$G_{II} = \frac{18P^2\left(a+\chi_{II}h_1\right)^2}{B^2E_{1f}} \frac{h_1h_2}{\left(h_1+h_2\right)^2 \cdot \left(h_1^3+h_2^3\right)} \tag{8}$$

$$\frac{G_I}{G_{II}} = \frac{h_1^2 \cdot (h_1+h_2)^2}{3h_2^4} \cdot \left[\frac{a+\chi_I h_2}{a+\chi_{II}h_1}\right]^2 \tag{9}$$

Where h_1 is the thickness of the free arm, h_2 the thickness of the loaded arm, and $\chi_{II} = 0.42\chi_I$.

The correction for the moment arm shortening is the same as the ELS test (Eq. 5, 6), except for the β parameter which changes to:

$$\beta = \left(\frac{h_1+h_2}{h_2}\right)^3$$

Asymmetric mixed-mode I+II: ADCB & MMF tests

For symmetric specimens, the Eq. (1,4,7,8) provide satisfactory results. These mode partitioning methods are based on the beam theory [9] and are usually called a global method. The mode decomposition seems to differ for non-symmetric specimens. Ducept et al. [4] have applied another partitioning approach to asymmetric delamination tests for composites. This approach [15] is based on the calculation of a stress intensity factor and usually referred to as a local method.

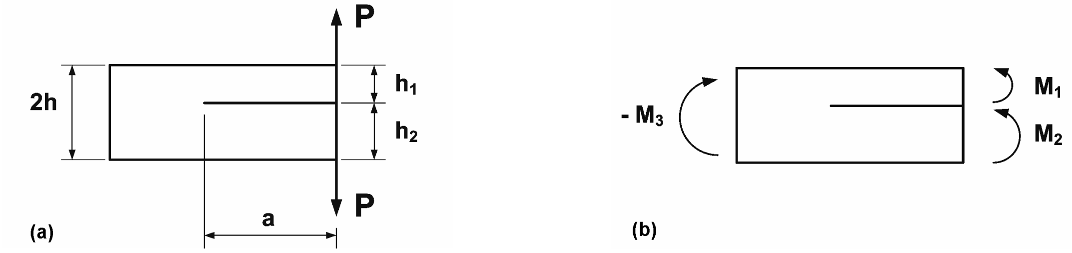

Fig. 3. ADCB specimen for local data reduction method. (a) Specimen under loads. (b) Resulting moments.

The Fig. 3 shows the schematic diagrams of an ADCB specimen. The resulting equations of the local method are reproduced as follows:

$$G_I = \frac{1}{2B^2E_{1f}}\left[\frac{F\cos(\omega)}{\sqrt{Ah_1}} + \frac{M\sin(\omega+\gamma)}{\sqrt{Ih_1^{\ 3}}}\right]^2 \tag{10}$$

$$G_{II} = \frac{1}{2B^2E_{1f}}\left[\frac{F\sin(\omega)}{\sqrt{Ah_1}} - \frac{M\cos(\omega+\gamma)}{\sqrt{Ih_1^{\ 3}}}\right]^2 \tag{11}$$

Where $F = -\frac{6h_1h_2}{(h_1+h_2)^3}\cdot M_3$, $\quad M = M_1 - \frac{h_1^{\ 3}}{(h_1+h_2)^3}M_3$,

$M_3 = M_1 + M_2$, $\quad M_1 = P_1 a$, $\quad M_2 = P_2 a$,

$A = \frac{1}{1+4(h_1/h_2)+6(h_1/h_2)^2+3(h_1/h_2)^3}$, $\quad I = \frac{h_2^{\ 3}}{12(h_1^{\ 3}+h_2^{\ 3})}$,

$\sin(\gamma) = \sqrt{AI}\cdot 6(h_1/h_2)^2\cdot(1+h_1/h_2)$, and $\quad \omega = 52.1 - 3(h_1/h_2)$

From Eq. (10,11), the G_I and G_{II} can be calculated using only the loading information (P_1, P_2, and a) and the thickness information (h_1 and h_2). The γ emerges when the ERR is written as a positive definite quadratic in terms of force and moment loads. The ω is a phase angle shift, in degree, when equating the stress intensity factor-derived ERR to the energy-derived ERR [16].

Table 1 compares the mode ratios, G_I/G_{II}, predicted by the global and local methods. While the results are in good agreement for symmetric MMF specimens, discrepancies exist for asymmetric specimens. The global method results in a very high mode I content in AMMF test and no mode II in ADCB test. These analytical mode ratios will be compared with the mode ratios obtained from finite element simulations.

Table 1
Mode ratios (G_I/G_{II}) of MMF, AMMF, and ADCB tests calculated by global and local methods.

Test	Global Method	Local Method
MMF	1.33	1.33
AMMF ($h_2/h_{total} = 1/3$)	12.00	1.55
ADCB ($h_2/h_{total} = 1/3$)	∞	5.39

The analytical calculation (Eq. 1,9,10,11) for UD specimens shows that the mode ratio depends largely on the thickness ratio of the two arms. Since we have not found any analytical solution specific for MD specimens, the asymmetric MD specimens were made with the same thickness ratio as the unidirectional AMMF and ADCB specimens. The MD mode ratios will also be determined from finite element simulations.

2.2. Stacking sequence

Stacking sequences for a delamination interface of 0°/45° were evaluated to minimize common concerns in fracture toughness test of multidirectional specimens. The classical lamination theory used here follows the notation of Hashin [17]. A specimen is considered to consist of three parts. Arm 1 and arm 2 are in the cracked region. The uncracked part is called arm 3. The three arms must have no in-plane/out-of-plane coupling i.e. the matrix $\boldsymbol{B}$ of the laminate is a zero matrix. The in-plane extensional/shear coupling must also be eliminated ($A_{16} = A_{26} = 0$). Stacking sequences without the aforementioned couplings were then determined and selected according to the criteria presented in the following paragraphs.

2.2.1. Energy release rate distribution along delamination front

Since the ERR varies across the specimen width [18], it is desirable to have relatively flat and symmetrically distributed ERR profile. Two non-dimensional parameters, D_c and B_t, are used to assess the ERR distribution. The D_c indicates the curvature due to longitudinal/transverse bending coupling. It is determined using the Eq. (12) with $D_c = 0.25$ as an upper bound [19].

$$D_c = \frac{{D_{12}}^2}{D_{11} D_{22}} \tag{12}$$

Where $\boldsymbol{D}_{ij}$ is a bending stiffness component in the $\boldsymbol{D}$ matrix of the laminate.

The B_t is defined in Eq. (13) [18]. This parameter indicates the skewness of the crack profile due to bending/twisting coupling of the specimen arms. It is recommend that B_t be kept minimum to minimize the skewness of the ERR profile.

$$B_t = \left| \frac{D_{16}}{D_{11}} \right| \tag{13}$$

2.2.2. Effect of residual stresses

Residual stresses arise from differential thermal shrinkage of laminate components when the laminate is cured at high temperature and then cooled down to room temperature. It is suggested that the entire effect of residual stresses in a DCB specimen is the external work effect originated from thermally induced curvature in the DCB arms [20]. As the delamination grows, the unbalanced arms may curve due to residual stresses, thus giving a residual displacement at the loading point. The residual effect disappears if both arms of the DCB specimen are symmetric laminates, which do not curve by residual stresses. Nairn [20] provided a complete formulation with examples thus any lay-up can be tested for the residual stress effect.

2.2.3. Global damage of the specimens

Energy dissipation can arise from global specimen damage and plastic deformation. This energy has to be taken into account to obtain the correct ERR. Ladevèze's damage mechanics application on composite materials has been implemented, through a specific material routine, into a finite element code SAMCEF© used at ENSICA [21]. An individual composite ply is modeled as an elasto-plastic damageable material. This material model takes into account the main intralaminar damages i.e. transverse cracking and fiber-matrix debonding, as well as the inelastic behavior of the ply. The model and experimental data were used to determine specimen damage.

2.2.4. Change of delamination plane

Delamination migration, the delamination crack repeatedly changing the propagation interface, are often observed for angle-ply interface, cross-ply interface, and UD interface when the intended delamination growth direction does not coincide with the fiber direction [7]. The migration is the result of matrix failure when an interface ply is under a tension load in directions other than the fiber direction. To have valid fracture toughness values of an interface, the change of delamination plane must be avoided. Our selected 0°/45° interface was tested with the 0° interfacing ply receiving higher tension load in order to minimize the risk of migration.

2.3. Resulting lay-up

The ply characteristics of the T700/M21 composite are shown below. E_{1f} is a flexure modulus determined from DCB and ELS test results. E_{22}, G_{12}, and ν_{12} were determined from traction tests on specimens with the lay-ups of 90°, ±45°, and 0° respectively. The UD prepreg is made by Hexcel Composites using T700GC carbon fiber and M21 epoxy matrix. This prepreg has 35% of resin content by weight.

E_{1f}: 98.62 GPa, E_{22}: 7.69 GPa, G_{12}: 4.75 GPa, ν_{12}: 0.33, Cured ply thickness 0.260 mm.

It was found that no 12-ply lay-up could meet the requirements. The number of plies was then increased to 18. The best resulting stacking sequence in terms of D_c and B_t is shown below, with "//" indicating the delamination interface.

0/45/-45/-45/45/0 // 45/0/-45/0/-45/-45/45/45/0/45/0/-45

The values of D_c, B_t, and residual stress effect, shown in Table 2, can be calculated analytically. However, the specimen damage and the delamination migration have to be verified after the experiment.

Table 2

D_c, B_t, and residual stress effect of the selected multidirectional stacking sequence.

	Arm 1 (12 plies)	Arm 2 (6 plies)	Arm 3 (18 plies)
D_c	0.181	0.063	0.187
B_t	0.000	0.064	0.003
Residual stress effect	0%	0%	0%

Note: D_c and B_t of a unidirectional specimen are 0.008 and 0.000 respectively.

2.4. Test specimens

Table 3 presents all specimen types used for the experiment. The resulting multidirectional specimens are called ADCB18M and AMMF18M for ADCB and AMMF tests. Two 18-ply UD specimens, ADCB18 and AMMF18, were added to avoid possible influences of specimen geometries in the ERR comparison. The nominal specimen dimensions, in parentheses, indicate (*Length, Width,* and *Initial crack length*) in millimeter.

Composite laminates were made by stacking 12 and 18 plies of the UD prepreg. An aluminium foil (13 µm) or a Teflon release film (12 µm) was used as an insert to create the initial delamination. The test data was taken 5 mm away from the insert tip hence the influence of insert type was ignored. The lay-ups were then polymerized in a thermo-regulated hydraulic press under 6 bars at two temperature steps: 135°C for 40 minutes and 180°C for 120 minutes. The temperature ramp was ± 3°C/min.

Table 3

Test specimens.

	Mode I	Mixed-mode	Mixed-mode	Mixed-mode	Mode II
12 Plies, UD	DCB (140x20x40)	ADCB12 (140x20x40)	AMMF12 (140x20x80)	MMF (140x20x80)	ELS (140x20x80)
18 Plies, UD		ADCB18 (170x20x80)	AMMF18 (140x20x80)		
18 Plies, MD		ADCB18M (170x20x80)	AMMF18M (140x20x80)		

Figure 4 shows typical ADCB and AMMF test configurations. The thinner arm (arm 2) is attached to the upper fixture and displays higher curvature than the thicker arm. The crosshead speed of all tests was 0.5 mm/min during delamination propagation.

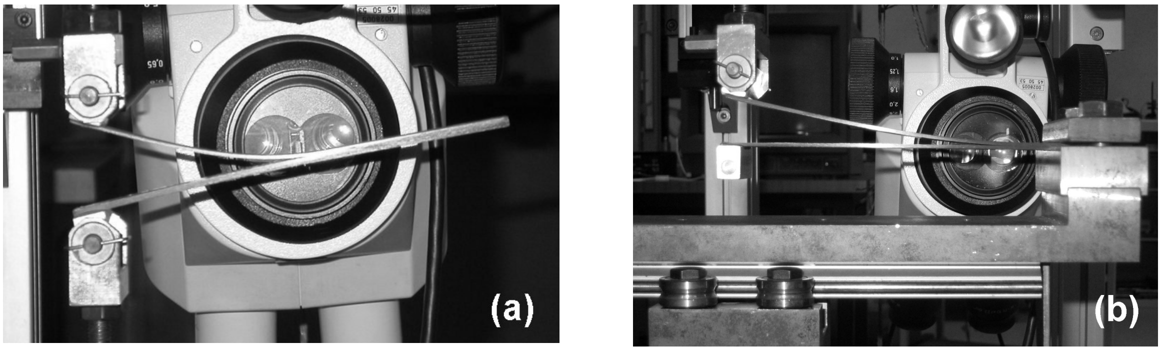

Fig. 4. Test configurations. (a) ADCB test. (b) AMMF test.

3. Numerical simulation

3.1. Determination of energy release rate

Two methods were used to determine the energy release rate.

3.1.1. Virtual crack extension (VCE) method

This method is a built-in feature of the finite element code SAMCEF. The node at the crack front is split into two, each one is attached to only one side of the crack. The nodes are then moved by a given distance. The ERR is calculated from the energy change of the surrounding elements with respect to the variation of crack length. The opening displacements and reaction forces at these nodes are used for mode partitioning calculation [22].

3.1.2. Virtual crack closure technique (VCCT)

The VCCT method gives the ERR at the crack front directly in three modes. It is based on the principle that the energy released when a crack is extended by a length Δa is identical to the energy required to close the crack back under the same external load. The method was implemented with a correction for large deformation [23].

3.2. Energy release rate distribution

Three-dimensional finite element models were used to determine the ERR distribution across the width of the specimens. A typical model is shown in Fig. 5. The model is created with 3D composite 20-node volume elements. The longitudinal mesh refinement around the crack front is made such that the element length is equal the prepreg's thickness. The refined zone is three times longer than the total thickness of the specimen. Four plies around the crack plane, in thickness direction, are modeled individually. The load blocks are modeled with rigid bodies. The ERRs are determined by the VCE method.

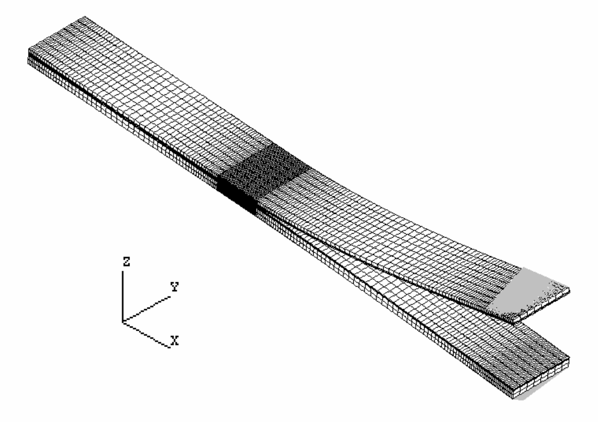

Fig. 5. Typical 3D finite element model of a test specimen.

3.3. Critical energy release rate

The values of the critical energy release rate were determined from two-dimensional finite element models using crack lengths and their corresponding critical forces from the experimental data. The models are created with 8-node elements under a plane strain assumption. Each ply of the specimens is modeled individually along the thickness. The longitudinal mesh refinement is identical to the 3D models. The VCE method was used in the models of all test configurations to determined the ERR values. The VCCT method was used in selected configurations, only to verify the reliability of the VCE method.

4. Validation of stacking sequence

Before analyzing the test results, a series of validation procedures was performed on the tested specimens.

4.1. Experimental observation

An X-ray imaging of an AMMF18M specimen is shown in Fig. 6a. The crack propagates from the insert tip, at the bottom, toward the final crack front at the top. The crack front seems symmetric, and does not show a pronounced curvature. Figure 6b shows the fracture surfaces of an ADCB18 specimen, on the left, and an ADCB18M specimen, on the right. The crack fronts are highlighted for clearness. The crack profile of the ADCB18 is flat and quite symmetric. The ADCB18M has a more curved and less symmetric profile. The loss of fiber bundles due to fiber bridging can be seen as dark vertical lines on these zero-degree surfaces. There is no indication of delamination migration.

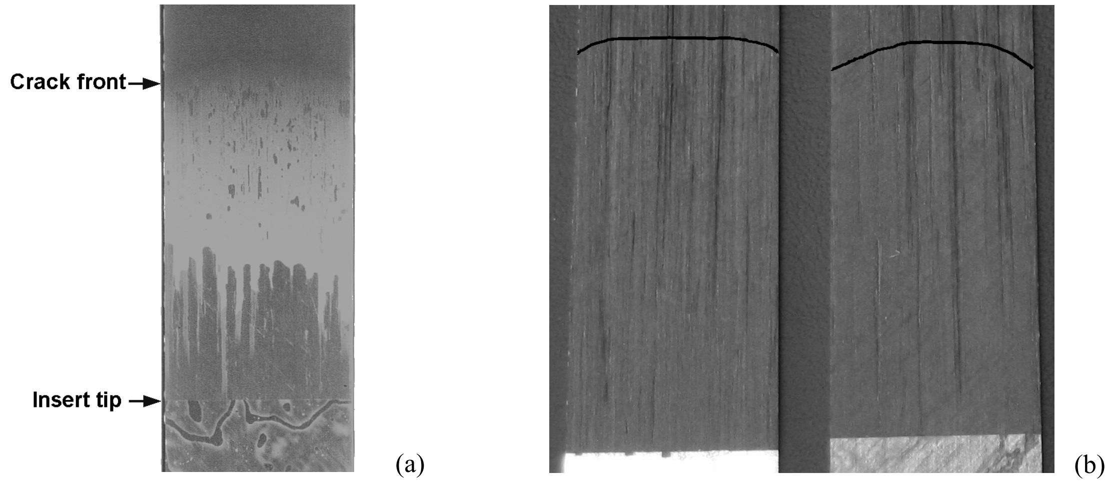

Fig. 6. Profiles of delamination fronts. (a) X-ray image of an AMMF18M specimen. (b) Fracture surfaces of an ADCB18 specimen (left) and an ADCB18M specimen (right).

Delamination migration is perhaps the greatest concern for the fracture toughness test of multidirectional interfaces. The fracture toughness of the intended interface cannot be determined if the delamination does not stay in the same plane during the test. Figure 7 shows a part of the cross-section of an AMMF18M specimen. The delamination separates the 0° interface ply, above, from the 45° interface ply as intended. Small random damages in the 0° interface ply are indicated by the arrows. This damage corresponds to the fiber bridging as discussed earlier. The irregular fiber distribution within the plies is typical for laminates made from this type of prepreg [24]. The observation of successive cross-sections shows that the delamination remains at the intended 0°/45° interface.

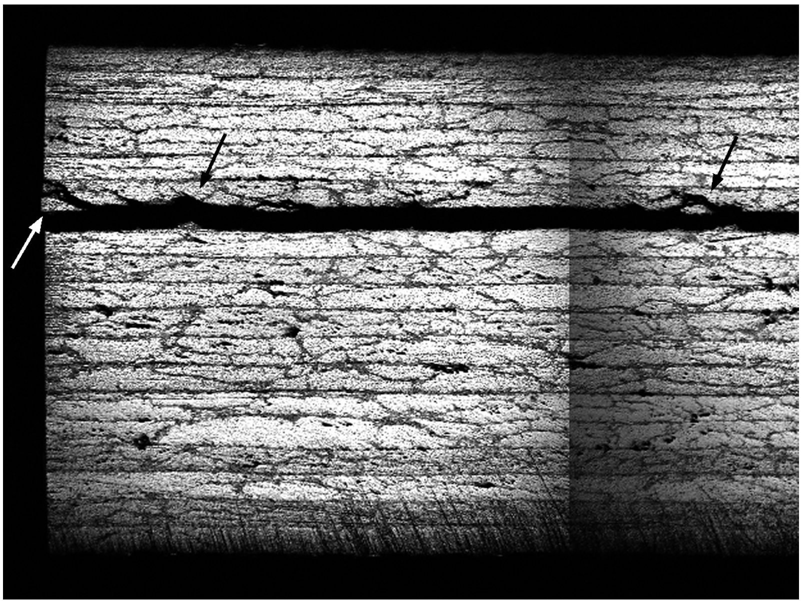

Fig. 7. Delamination in an AMMF18M specimen creates random damages in the 0° interface ply

4.2. Energy release rate distribution along delamination front

The ERR distributions are obtained from 3D finite element models using VCE method. Figure 8 shows the plots of normalized total ERR across the specimen width. The two symmetric curves (dotted lines) are from ADCB18 and AMMF18 specimens. Since the D_c value of the UD lay-up is much lower, the curves are clearly flatter than those of MD specimens. The D_c and B_t values of the ADCB18M and AMMF18M specimens are identical since they are made from the same stacking sequence. Both specimens have similar skewness, but the ADCB18M has more pronounced curvature due to the influence of D_c from both arms. Qualitatively, the differences between the UD and MD distributions correspond well with the crack front profiles observed in Fig. 6b.

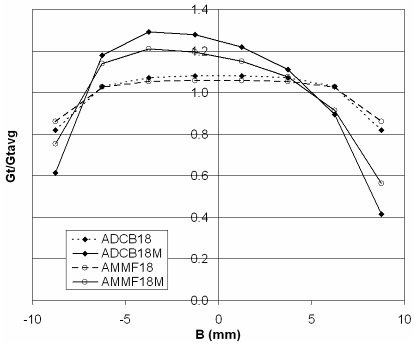

Fig. 8. Normalized total energy release rates of asymmetric 18-ply specimens.

4.3. Global laminate degradation

The elasto-plastic damageable behavior of the material is illustrated in Fig. 9. The MD lay-up of the arm 2 is modeled by 2D shell elements. The specimen is fixed at one end and loaded at the other end with an increasing cyclic traction force. The resulting force-displacement diagram shows both the degradation of the laminate i.e. a progressive decrease of the elastic modulus, and the plastic deformation which results in residual displacements.

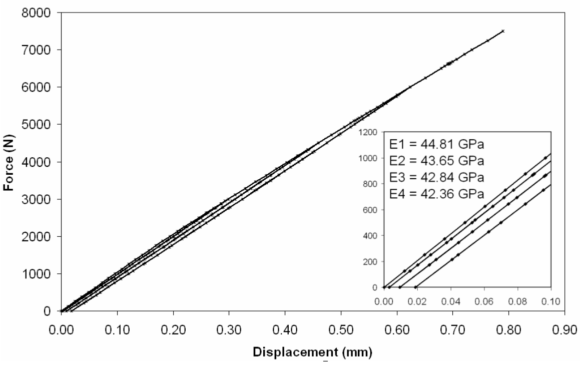

Fig. 9. Force-displacement diagram demonstrating elasto-plastic damageable material behavior.

When this material behavior is applied to the fracture toughness models, each arm of the specimen (defined in 2.3.) is modeled as a cantilever beam. The delamination lengths and their corresponding critical forces are obtained from the experimental results. Figure 10 shows a simulation result of arm 2 loaded by two load-unload cycles. There is neither lost of rigidity nor residual displacement in the resulting force-displacement diagram.

Similar results were obtained from the models of the other arms. Therefore, the specimen is free of global ply damage and no energy is dissipated through this mechanism.

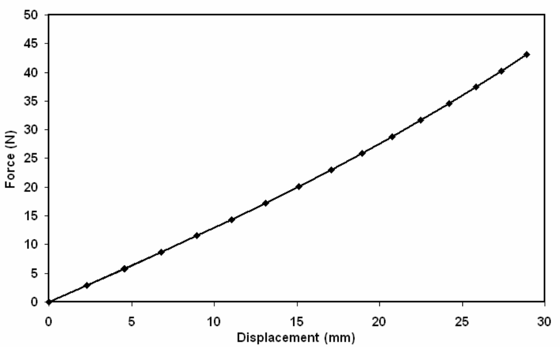

Fig. 10. Force-displacement diagram of the arm 2 model, using damageable material, shows no energy dissipation.

5. Results and discussion

5.1. Force-displacement results

The results of each test configuration were obtained by averaging the critical forces and displacements corresponding to each crack length. A range of the average results was then selected for the finite element simulations. Table 4 and 5 report the average experimental load and displacement values as well as the displacements obtained from the finite element models. The VCE and VCCT models predict identical displacement, thus shown together as δ FE. The correlation between the FE and the experimental results is reasonably good. The average displacement difference between experimental and FE values is less than 12% for the worst case. Compared to the dispersion of the test results, the difference is less one standard deviation for the majority of the test configurations.

Table 4

Average experimental loads and displacements compared with FE values – $a_0 = 40$ mm.

	a (mm)	45	50	55	60	65
DCB	P (N)	51.19	49.63	47.61	46.27	45.11
	δ EXP (mm)	5.76	7.41	9.35	11.16	13.31
	δ FE (mm)	5.58	7.27	9.12	11.33	13.85
ADCB12	P (N)	41.98	40.75	40.73	39.72	37.20
	δ EXP (mm)	8.06	10.35	13.01	16.02	19.01
	δ FE (mm)	8.07	10.53	13.72	17.06	20.07

Table 5

Average experimental loads and displacements compared with FE values – $a_0 = 80$ mm.

	a (mm)	85	90	95	100	105
AMMF12	P (N)	27.92	28.32	27.98	28.19	27.75
	δ EXP (mm)	28.17	31.92	34.74	38.97	42.65
	δ FE (mm)	30.30	34.41	38.15	42.58	46.56
MMF	P (N)	50.38	50.88	51.50	49.67	50.40
	δ EXP (mm)	20.54	23.26	25.87	27.33	29.88
	δ FE (mm)	23.14	25.61	28.37	30.18	33.41
ELS	P (N)	110.66	106.14	101.62	95.67	91.27
	δ EXP (mm)	36.25	36.33	36.41	36.87	37.29
	δ FE (mm)	34.81	35.61	36.46	36.88	37.82
ADCB18	P (N)	34.17	31.93	31.31	29.56	28.73
	δ EXP (mm)	13.60	14.96	16.98	18.73	20.80
	δ FE (mm)	13.27	14.64	16.76	18.36	20.54
ADCB18M	P (N)	26.21	25.17	24.82	24.28	22.83
	δ EXP (mm)	15.01	16.93	19.32	22.37	23.87
	δ FE (mm)	13.23	14.98	17.24	19.54	21.19
AMMF18	P (N)	47.27	44.03	38.80	38.04	36.31
	δ EXP (mm)	17.46	18.58	19.18	20.76	22.13
	δ FE (mm)	17.51	18.78	19.09	21.25	23.00
AMMF18M	P (N)	45.45	44.46	43.19	43.17	43.15
	δ EXP (mm)	23.50	26.15	28.62	31.35	34.07
	δ FE (mm)	21.40	23.73	26.06	29.19	32.53

5.2. Total energy release rate

For the ADCB18 specimen, the total energy release rates determined from the global, local, VCE, and VCCT methods are in excellent agreement (Table 6). Additionally, a simplified area method was used to double-check the values from the analytical and finite element methods. An average ERR between two crack lengths is determined from the force-displacement diagram by adding the trapezoidal area between the two delamination points to the triangular area made by the first point and the origin of the diagram. The sum is then subtracted by the triangular area of the second crack point. The results are expected to oscillate around reasonable ERR values, which is the case for ADCB18.

The analytical calculations for multidirectional specimens were carried out using homogenized properties of the lay-up. However, this approach does not seem to produce good results since the total ERR values from the global and local methods differ greatly from the values obtained by the VCE and VCCT methods, as shown in Table 7 and 8. The finite element methods are believed to be more reliable because their results correlate well with the results from the simplified area method.

Table 6

Energy release rate and mixed-mode ratio – ADCB18

	a (mm)	85	90	95	100	105
Global method	G_t (J/m^2)	380.3	372.2	398.9	393.8	410.1
	G_I/G_t (%)	100	100	100	100	100
Local method	G_t (J/m^2)	380.3	372.2	398.9	393.8	410.1
	G_I/G_t (%)	84.4	84.4	84.4	84.4	84.4
VCE method	G_t (J/m^2)	373.6	364.3	388.0	381.8	395.8
	G_I/G_t (%)	87.7	87.6	87.6	87.6	87.6
VCCT method	G_t (J/m^2)	388.6	379.0	403.3	395.9	413.7
	G_I/G_t (%)	86.2	86.1	86.1	86.0	86.1
Area method	G_t (J/m^2)	385.7	367.4	423.4	383.5	390.0

Table 7

Energy release rate and mixed-mode ratio – ADCB18M

	a (mm)	85	90	95	100	105
Global method	G_t (J/m^2)	501.0	518.1	561.3	595.1	579.8
	G_I/G_t (%)	100	100	100	100	100
Local method	G_t (J/m^2)	501.0	518.1	561.3	595.1	579.8
	G_I/G_t (%)	84.4	84.4	84.4	84.4	84.4
VCE method	G_t (J/m^2)	287.5	295.7	318.5	335.9	326.4
	G_I/G_t (%)	94.6	94.6	94.6	94.6	94.6
VCCT method	G_t (J/m^2)	297.1	305.9	329.5	347.4	338.3
	G_I/G_t (%)	93.9	93.9	93.9	93.9	93.9
Area method	G_t (J/m^2)	330.1	329.7	430.9	344.6	403.4

Table 8

Energy release rate and mixed-mode ratio – AMMF18M

	a (mm)	85	90	95	100	105
Global method	G_t (J/m^2)	1214.0	1286.0	1338.2	1464.3	1595.4
	G_I/G_t (%)	92.3	92.3	92.3	92.3	92.3
Local method	G_t (J/m^2)	1289.3	1383.1	1454.3	1609.9	1773.1
	G_I/G_t (%)	60.8	60.8	60.8	60.8	60.8
VCE method	G_t (J/m^2)	647.9	686.3	713.3	775.7	838.5
	G_I/G_t (%)	74.7	74.6	74.6	74.6	74.6
VCCT method	G_t (J/m^2)	658.2	696.9	724.4	787.5	851.1
	G_I/G_t (%)	71.2	71.1	71.0	71.0	71.0
Area method	G_t (J/m^2)	719.4	715.5	591.3	591.3	726.5

5.3. Mode decomposition

For asymmetric unidirectional specimens, mode partitioning by the local method seems to provide satisfactory results while the global method is not quite suitable. Both partitioning results are compared with the FE results in Table 6. The two methods, however, work equally well for symmetric unidirectional specimens.

Since homogenized properties are used for the analytical calculations, the multidirectional specimens are equivalent to unidirectional specimens with a new set of properties. The analytical mode partitioning results are identical to the results of the original UD specimens. Table 7 and 8 show certain discrepancies between the local method and the finite element methods. Knowing that the local method was unable to predict a correct value of the total ERR and that the mode partitioning made no difference between UD and MD lay-ups, the mode partitioning by finite element methods is taken as more relevant.

Figure 11 compares the mode decomposition of all asymmetric specimens. The local method is used for analytical approach and the VCE method for finite element approach.

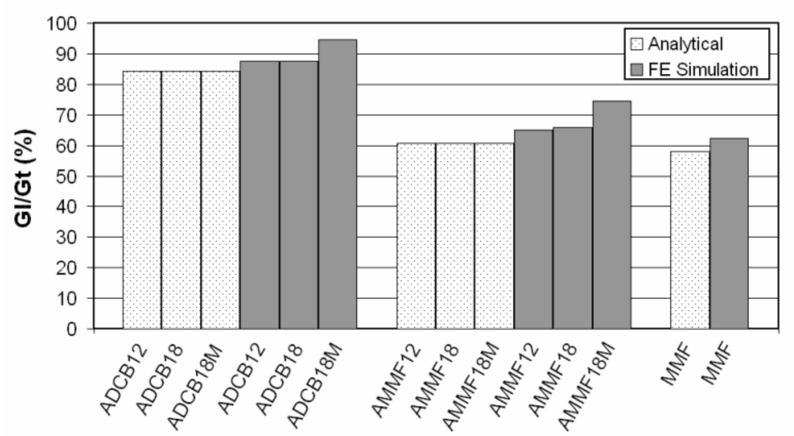

Fig. 11. Mode partitioning of asymmetric specimens, analytical and FE results.

5.4. Delamination propagation criteria

The energy release rates of the UD specimens resulted from the local and VCE methods are plotted in the G_I-G_{II} chart as shown in Fig. 12. For symmetric specimens, analytical values (solid diamond) are in excellent agreement with FE values (cross). The VCE method predicts slightly higher mode I content than the local method for the MMF test. Good correlations are obtained again for ADCB12 (diamond), ADCB18 (square), and AMMF18 (triangle) tests. The ERR values of the AMMF12 (circle) show some discrepancies. The possible cause is that the loaded arm of the AMMF12 is very thin, consisting of only 4 plies. The non-linearity of the force-displacement diagram might affect the analytical calculation. The mode ratios, however, are consistent with those of the AMMF18.

While the results of the 12-ply specimens seem to fit well with the usual power law criterion [25], shown in Eq. 14, the ERR values of the 18-ply specimens are noticeably lower than the values of their 12-ply counterparts. The 18-ply specimens were made from a different batch of prepreg; however, we would like to investigate further before attributing the difference solely to the batch variation. The specimen thickness and fiber bridging could have influences on the ERR values and the R-curves. Since the interfacing plies are 0° for both thicknesses, the forces attributed to the fiber bridging could be assumed to be equal. The proportion of these forces in the total forces measured from the tests is, however, higher for the 12-ply specimens. Thus, we believe that the total force is dominated by the force to overcome the specimen rigidity for the 18-ply specimens while the fiber bridging force still has an influence on the less rigid, 12-ply specimens. As a result, figure 12 shows long lines for 12-ply specimens tested with opening displacements, indicating steep R-curves. Moreover, possible uncertainties from moment-arm shortening are more limited in 18-ply specimens due to their higher rigidities.

$$\left(\frac{G_I}{G_{IC}}\right)^{\alpha}+\left(\frac{G_{II}}{G_{IIC}}\right)^{\beta}=1 \tag{14}$$

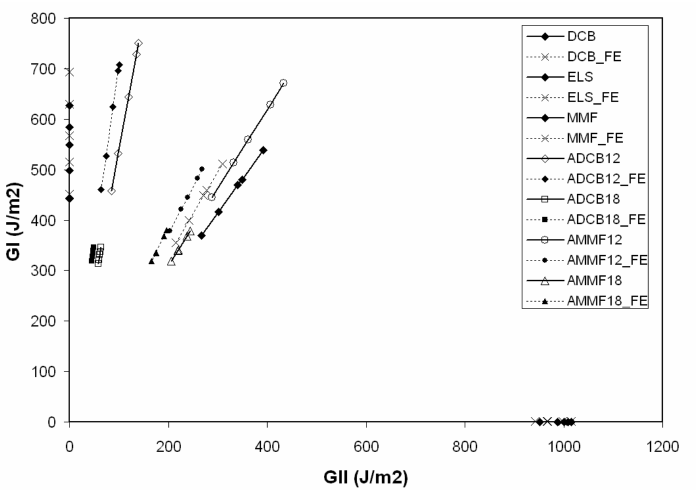

Fig. 12. Delamination propagation envelope of UD lay-up: comparison of analytical and FE results.

The experimental data of the multidirectional specimens can only be analyzed by the finite element methods. The results of the ADCB18M (hollow square) and AMMF18M (hollow triangle) are shown in Fig. 13, together with the FE results of the unidirectional specimens. The transition from UD to MD lay-up creates conflicting results as the total ERR decreases for the ADCB18M, but increases for the AMMF18M. There is no immediate interpretation since we only have two test configurations. More multidirectional tests at different mode ratios have to be performed to complete the fracture envelope and to explain the present results.

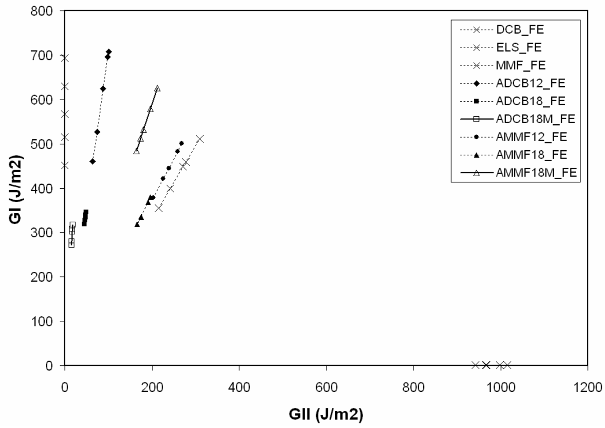

Fig. 13. Partial delamination propagation criteria: comparison of UD and MD lay-ups.

6. Conclusions

In an attempt to establish propagation criteria for the delamination between plies of different orientations, the ADCB test appears to be a suitable configuration for a test at very high mode I ratios. The widely used DCB test was avoided due to anticipated problems with intralaminar damage developing at the ply interface of interest. The procedure used for choosing the stacking sequence in this present work resulted in desirable propagation behavior of the delamination. There was no change of delamination plane, an acceptable crack front profile, no initial specimen curvature, and no energy dissipation through global specimen damage.

The finite element and analytical methods resulted in consistent energy release rate and mode partitioning for the unidirectional specimens. The local method was more suitable than the global method for asymmetric specimens. For the multidirectional specimens, the experimental data can only be analyzed by the finite element methods. To have more reliable energy release rate and mode partitioning results, the correlation between FE models and experimental results of UD specimens should first be established. Analyses of MD experiments can then be performed by modifying the lay-up of the UD-calibrated models.

More tests at lower mode I ratios and pure mode II have to be performed to produce a reliable delamination propagation criterion for 0°/45° interface. This criterion can then be used to determine the pure mode I fracture toughness.

References

[1] Hiley MJ. Delamination between multi-directional ply interfaces in carbon-epoxy composites under static and fatigue loading. In: Williams JG, Pavan A, editors. Fracture of polymers, composites, and adhesives. Elsevier, 2000. p. 61-72.

[2] Tao J, Sun CT. Influence of ply orientation on delamination in composite laminates. J Composite Mater. 1998;32(21):1933-1947.

[3] Kinloch AJ, Wang Y, Williams JG, Yayla P. The mixed-mode delamination of fiber composite materials. Composites Sci Tech. 1993;47(3):225-237.

[4] Ducept F, Gamby D, Davies P. A mixed-mode failure criterion derived from tests on symmetric and asymmetric specimens. Composites Sci Tech. 1999;59(4):609-619.

[5] Mezière Y, Michel L, Carronnier D. Mixed-mode delamination failure criteria in carbon fibre/composite under quasi-static and cyclic loading. In: Williams JG, Pavan A, editors. Fracture of polymers, composites, and adhesives. Elsevier, 2000. p. 97-110.

[6] Gong XJ. Rupture interlaminaire en mode mixte I+II du composite stratifié verre/époxy unidirectionnel et multidirectionnel. PhD thesis. Compiègne: Université de Technologie de Compiègne, 1992.

[7] Andersons J, König M. Dependence of fracture toughness of composite laminates on interface ply orientations and delamination growth direction. Composites Sci Tech. 2004;64(13-14):2139-2152.

[8] Sundararaman V, Davidson BD. An unsymmetric double cantilever beam test for interfacial fracture toughness determination. Int J Solids Structures. 1997;34(7):799-817.

[9] Williams JG. Fracture mechanics of anisotropic materials. In: Friedrich K, editor. Application of fracture mechanics to composite materials. Elsevier, 1989. p. 3-38.

[10] Hashemi S, Kinloch AJ, Williams JG. The analysis of interlaminar fracture in uniaxial fibre-polymer composites. Proc R Soc Lond. 1990;A427:173-199.

[11] Hashemi S, Kinloch AJ, Williams JG. The effects of geometry, rate and temperature on the mode I, mode II and mixed-mode I/II interlaminar fracture of carbon-fiber/poly(ether-ether ketone) composites. J Composite Mater. 1990;24:918-956.

[12] Williams JG. The fracture mechanics of delamination tests. J Strain Analysis. 1989;24(4):207-214.

[13] ASTM. Standard test method for mode I interlaminar fracture toughness of unidirectional fiber-reinforced polymer matrix composites. 1994;D 5528-94a.

[14] Davies P, Blackman BRK, Brunner AJ. Mode II delamination. In: Moore DR, Pavan A, Williams JG, editors. Fracture mechanics testing methods for polymers, adhesives, and composites. Elsevier, 2001. p. 307-333.

[15] Hutchinson JW, Suo Z. Mixed mode cracking in layered materials. In: Advances in applied mechanics, Vol.29. Academic Press, 1992. p. 63-191.

[16] Suo Z. Delamination specimens for orthotropic materials. J Applied Mech. 1990;57:627-634.

[17] Hashin Z, Rosen BW, Humphreys EA, Newton C, Chaterjee S. Fiber composite analysis and design: Composite materials and laminates, Volume I. Washington DC: Federal Aviation Administration, Report No. DOT/FAA/AR-95/29, 1997.

[18] Sun CT, Zheng S. Delamination characteristics of double-cantilever beam and end-notched flexure composite specimens. Composites Sci Tech. 1996;56:451-459.

[19] Davidson BD, Krüger R, König M. Effect of stacking sequence on energy release rate distributions in multidirectional DCB and ENF specimens. Engng Fracture Mech. 1996;55(4):557-569.

[20] Nairn JA. Energy release rate analysis for adhesive and laminate double cantilever beam specimens emphasizing the effect of residual stresses. Int J Adhesion Adhesives. 1999;20:59-70.

[21] Lachaud F. Délaminage de matériaux composites à fibres de carbone et à matrices organiques: Etude numérique et expérimentale, suivi par émission acoustique. PhD thesis. Toulouse: ENSICA, 1997.

[22] SAMCEFv11.0 user’s manual. Samtech, 2003.

[23] Krueger R. The virtual crack closure technique: History, approach and applications. Maryland: NASA Center for Aerospace Information, ICASE Report No. 2002-10, 2002.

[24] Prombut P. Caractérisation du délaminage pour des stratifies de T700/M21. In: Benzeggagh ML, Lamon J, editors. Comptes rendus des quatorzièmes journées nationales sur les composites, Vol.3. AMAC, 2005. p. 1033-1041.

[25] Reeder JR. An evaluation of mixed-mode delamination failure criteria. NASA technical memorandum 104210, 1992.

Figure captions

Fig. 1. Load block dimension.

Fig. 2. Specimen shortening in ELS and MMF tests.

Fig. 3. ADCB specimen for local data reduction method. (a) Specimen under loads. (b) Resulting moments.

Fig. 4. Test configurations. (a) ADCB test. (b) AMMF test.

Fig. 5. Typical 3D finite element model of a test specimen.

Fig. 6. Profiles of delamination fronts. (a) X-ray image of an AMMF18M specimen. (b) Fracture surfaces of an ADCB18 specimen (left) and an ADCB18M specimen (right).

Fig. 7. Delamination in an AMMF18M specimen creates random damages in the 0° interface ply

Fig. 8. Normalized total energy release rates of asymmetric 18-ply specimens.

Fig. 9. Force-displacement diagram demonstrating elasto-plastic damageable material behavior.

Fig. 10. Force-displacement diagram of the arm 2 model, using damageable material, shows no energy dissipation.

Fig. 11. Mode partitioning of asymmetric specimens, analytical and FE results.

Fig. 12. Delamination propagation envelope of UD lay-up: comparison of analytical and FE results.

Fig. 13. Partial delamination propagation criteria: comparison of UD and MD lay-ups.

Tables

Table 1: Mode ratios (G_I/G_{II}) of MMF, AMMF, and ADCB tests calculated by global and local methods.

Table 2: D_c, B_t, and residual stress effect of the selected multidirectional stacking sequence.

Table 3: Test specimens

Table 4: Average experimental loads and displacements compared with FE values – a0 = 40 mm.

Table 5: Average experimental loads and displacements compared with FE values – a0 = 80 mm.

Table 6: Energy release rate and mixed-mode ratio – ADCB18

Table 7: Energy release rate and mixed-mode ratio – ADCB18M

Table 8: Energy release rate and mixed-mode ratio – AMMF18M